Bulk and surface characteristics of pure and alkalized Mn_2O_3 : TG, IR, XRD, XPS, specific adsorption and redox catalytic studies†

Mohamed I. Zaki,* Muhammd A. Hasan, Lata Pasupulety and Kamlesh Kumari

Chemistry Department, Faculty of Science, Kuwait University, P.O. Box 5969, Safat 13060, Kuwait

α-Mn_2O_3 (containing a minor proportion of Mn_5O_8) was obtained by calcination of pure MnO_2 at 700 °C for 2 h. It was alkalized by impregnation of the parent dioxide with potassium and barium nitrate solutions prior to the calcination. K-Mn_2O_3 (α-Mn_2O_3 + KMn_8O_{16}) and Ba-Mn_2O_3 (α-Mn_2O_3) thus respectively produced were subjected, together with the unmodified Mn_2O_3, to the title bulk and surface characterization techniques. It has been implied that the alkalization improves the electron density and the mobility of lattice and surface oxygen species. As a result, the bulk thermochemical stability is reduced on heating in a CO atmosphere, and a capacity towards CO_2 uptake is developed. Moreover, the surface catalytic behaviour towards CO oxidation in the gas phase is maintained, and the behaviour towards H_2O_2 decomposition in the liquid phase is considerably promoted.

Che and Tench,[1,2] Kung and Kung[3] and Gellings and Bouwmeester[4] have reviewed the results of several studies on the nature and reactivity of surface oxygen species involved in oxidation catalysis on metal oxides. The discussion presented by these authors can help to conclude that the catalyst selectivity is largely governed by the nature of the surface oxygen species involved. Broadly speaking, lattice oxygen sites (O^{2-}) are considered to lead essentially to selective oxidation, whereas adsorbed oxygen species (O_2^{x-}, O^- and O^{2-}) lead to deep oxidation. Specifically, however, electron-poor (electrophilic) oxygen species (O_2^{x-} and O^-) are shown to be more reactive in deep oxidation processes than electron-rich (nucleophilic) species (O^{2-}). The abundance of either of these two types of oxygen species (electrophilic and nucleophilic) on the surface has been found to be determined by the oxide bulk composition and semiconductive properties.[5,6] Whereas p-type semiconductive oxides, such as NiO, MnO and Mn_3O_4, form dominantly nucleophilic adsorbed oxygen species, n-type oxides, such as ZnO, TiO_2 and Mn_2O_3, form preferentially electrophilic adsorbed species. In contrast, binary oxides in which lattice oxygen is involved in well-defined oxyanions, for example $Bi_2O_3 \cdot MoO_3$, do not form adsorbed oxygen species but only O^{2-} anions, which are nucleophilic.

In recent years, the search for deep oxidation (combustion) catalysts has been urged by environmental necessities.[4,7] Primarily, there is the need to reduce emission levels of harmful materials (CO, NO, soot and unburnt hydrocarbons) in the exhaust of the combustion of fossil fuel in vehicles and power plants.[8,9] The present study material, Mn_2O_3, is amongst the metal oxides nominated for the adequate chemical makeup of deep oxidation catalysts.[4,7] It has been proven competent in catalyzing a number of technologically and industrially important oxidation reactions.[10–13] Moreover, it enjoys a pronounced thermal stability (up to 950 °C),[14] has a surface-to-bulk compositional intimacy,[15] and exhibits n-semiconductive behaviour.[16] It also (*i*) exists in various structural modifications (α, β and γ),[17] (*ii*) concedes extensive defect structures[17] and (*iii*) tolerates reversible deoxygenation–oxygenation cycles (at 600–1000 °C).[18] These characteristics suit operational conditions of, and fulfil requirements for, automobile exhaust catalytic converters.[19] A chemical modification (alkalization), effected by K and Ba ion additives, was carried out in hope of revealing the bulk relationship with the surface performance in specific adsorption (CO and O_2) and catalytic (CO oxidation and H_2O_2 decomposition) experiments.

† *Non-SI units employed*: torr ≈ 133.3 Pa, eV ≈ 1.6×10^{-19} J

Experimental

Materials

A 99.9% pure Fluka (Switzerland) MnO_2 powder was the parent compound for the present study materials. It was calcined at 700 °C for 2 h in a dynamic atmosphere of air (50 cm^3 min^{-1}) to obtain pure Mn_2O_3.[14] It was also impregnated at ambient temperature with aqueous solutions of AR grade KNO_3 and $Ba(NO_3)_2$ (BDH, UK), dried at 100 °C for 48 h, and then calcined at 700 °C for 2 h to produce Mn_2O_3 modified (alkalized) with potassium (denoted K-Mn_2O_3) and barium (Ba-Mn_2O_3) at 5 wt% of the modifier (K and Ba). The impregnation was carried out by sprinkling a 15 g portion of MnO_2 onto 150 mL of the impregnating solution while magnetically stirring for 30 min. The resulting suspension was left to settle overnight, and then the solvent was removed by evaporation. The pure and modified Mn_2O_3 samples thus obtained were ground to <250 mesh and stored over silica gel till further use. It is worth noting that the material contents of K and Ba were not analytically controlled.

Methods

Thermogravimetry (TG). Non-cyclic TG was conducted while heating (at 10 °C min^{-1}) small portions (20 ± 1 mg) of test materials up to 1100 °C in a dynamic atmosphere (50 cm^3 min^{-1}) of pure O_2, or CO, or of a mixture of them (CO + O_2) in a 1 : 2 mass ratio. A model TGA-50 Shimadzu automatic analyzer (Japan), equipped with a TA-50WS work station for data acquisition and handling, was employed. The gases were 99.99% pure products of KOAC (Kuwait) and were used as supplied.

Cyclic TG was measured by heating test materials (at 10 °C min^{-1}) in 50 cm^3 min^{-1} of pure O_2 to 900 °C, followed by cooling at the same rate to 500 °C. The heating–cooling cycle was carried out twice in succession.

X-ray powder diffractometry (XRD). XRD was performed at ambient temperature, on a Siemens D5000 diffractometer (Germany) using Ni-filtered CuKα radiation (λ = 1.5418 Å, 40 kV, 30 mA), in the 2θ range between 10° and 80° with a divergence slit of 1°. An on-line microcomputer facilitated data acquisition and handling. For phase identification purposes, automatic JCPDS library search (standard search software) and match (standard DIFFRAC AT software) were carried out.

Infrared absorption spectroscopy (IR). IR was measured for KBr supported test samples (<1 wt%) over the frequency range of 4000–400 cm^{-1} and at a resolution of 4 cm^{-1}, using a model 2000 Perkin–Elmer FT spectrometer (UK). An on-line data station facilitated spectra acquisition and handling.

X-ray photoelectron spectroscopy (XPS). XPS spectra were recorded on a model VG Scientific 200 (UK) spectrometer using AlKα radiation (1486.6 eV) operating at 300 W, 13 kV and 23 mA. The spectra acquisition and handling were carried out by means of an on-line Eclipse data system (UK). The test materials were compacted onto the sample holder (8 mm in diameter) in an ambient atmosphere, mounted and stored in the introduction chamber until a vacuum of 10^{-9}–10^{-10} torr was reached (1 torr ≈133.3 Pa), and then transferred into the analysis chamber for data acquisition (0.2 eV step, 250 ms dwell time, 0.7 eV resolution, up to 10 scans). All binding energy values (BE/eV) were determined with respect to the C(1s) line (284.6 eV) originating from adventitious carbon, and the standard deviation of the peak position is estimated to be ±0.02 eV. The surface atomic percentage (%) of the elements observed was calculated from the peak areas (in counts eV s^{-1}) with integral subtraction of the background.

Gas sorpometry. Isothermal adsorption measurements of N_2, CO and O_2 on test materials were performed with an automatic ASAP 2010 Micromeritics sorpometer (USA) having a pressure measurement capacity of up to 950 torr and a reading resolution of 0.0005 torr. It is equipped with an on-line data acquisition and handling system operating a BET analytical software of adsorption isotherms, and an outgassing platform. The adsorptive gases (99.999% pure) were products of KOAC (Kuwait). Small portions of test materials (500 ± 2 mg) were outgassed at 200 °C for 3 h, then N_2 adsorption at liquid nitrogen temperature (−196 °C) was followed up to $P_{N2} = 300$ torr (*i.e.*, $P/P^\circ \simeq 0.4$) and the specific surface area ($S_{BET}/m^2\ g^{-1}$) was determined. This was followed by adsorbent outgassing at ambient temperature for 2 h and CO adsorption was then followed (at −196 °C) up to $P_{CO} = 150$ torr. A subsequent outgassing was carried out at the adsorption temperature (−196 °C) for 2 h and CO re-adsorption was similarly followed. Fresh portions of the adsorbents were mounted, outgassed at 200 °C for 2 h, and O_2 adsorption at 200 °C was followed up to $P_{O2} = 150$ torr. Then the adsorbents were re-outgassed (at 200 °C for 2 h) and O_2 re-adsorption was followed at the same temperature (200 °C). The data obtained facilitated determination of the surface monolayer capacity of chemisorbed CO (at −196 °C) and O_2 (at 200 °C).

H_2O_2 catalytic decomposition gasometry. The redox catalytic activity of the test materials was measured towards H_2O_2 decomposition in solution ($H_2O_2 \rightarrow H_2O + \frac{1}{2}O_2$). The reaction kinetics were followed isothermally at four different temperatures (20–35 °C) by determining the volume of oxygen released (V_t) as a function of time (up to 30 min), using a known mass of the test material (20–50 mg), 10 mL of diluted H_2O_2 solution (1 vol., Aldrich, USA) and a home-made gasometer similar to that described by Deren *et al.*[20] The results were corrected for self-decomposition of H_2O_2. Arrhenius parameters were determined, using the first-order kinetic equation:[21] $kt = \ln V_\infty - \ln (V_\infty - V_t)$, where V_∞ is the volume of O_2 released when all of the H_2O_2 is decomposed.

Results and Discussion

Bulk composition and crystalline structure

IR spectra taken from the calcination products of pure and impregnated MnO_2 samples are compared with a spectrum taken from commercial α-Mn_2O_3 (99.9% pure Fluka product) in Fig. 1. The diagnostic frequencies of the IR absorptions of α-Mn_2O_3 (at 668, 651, 598, 575, 525, 498, 451 and 411 cm^{-1}) are well-represented in the spectra of the three calcination products. However, the characteristic relative intensities are satisfactorily maintained only in spectrum (*c*) of the calcination product of $Ba(NO_3)_2$. The other two spectra [(*a*) and (*b*)] display the absorptions at 598 and 498 cm^{-1} with obviously stronger intensities, and spectrum (*a*) shows an additional strong absorption at 436 cm^{-1}. These results may show the calcination product of $Ba(NO_3)_2$–MnO_2 to consist solely of α-Mn_2O_3, whereas those of MnO_2 and KNO_3–MnO_2 to additionally contain other MnO_x species. According to Nohman *et al.*,[14] the modifications observed in the IR spectrum (*b*) of the calcination product of KNO_3–MnO_2 can account for the coexistence of cryptomelane- (KMn_8O_{16}) and manganoxide-like (Mn_5O_8) compositions, whereas those mon-

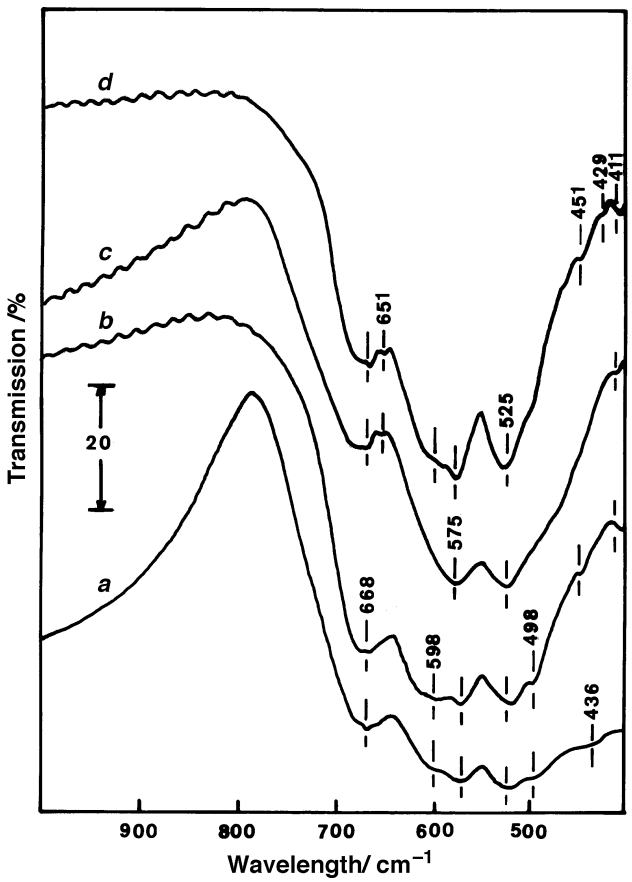

Fig. 1 KBr supported FT-IR spectra taken from the 700 °C calcination products of (*a*) MnO_2, (*b*) KNO_3–MnO_2 and (*c*) $Ba(NO_3)_2$–MnO_2. (*d*) α-Mn_2O_3 standard spectrum is included for comparison purposes

itored in spectrum (*a*) of the product of pure MnO_2 may reveal the coexistence of the manganoxide-like composition. The IR absorption band structure exhibited by the calcination products of the impregnated MnO_2 samples can help neither to confirm, nor to deny, the presence of separate KO_x and BaO_x species.[22]

XRD results, presented in the form of diffraction patterns (I/I_0 *vs.* *d* spacing/Å) derived from the resulting powder diffractograms (*I vs.* 2θ), exhibit very similar diffraction patterns for the calcination products of MnO_2 and $Ba(NO_3)_2$–MnO_2 [Fig. 2, (*a*) and (*b*)], which are assignable to weakly crystalline, Bixbyite-like α-Mn_2O_3. On the other hand, the diffraction pattern [Fig. 2, (*c*)] determined for the calcination product of KNO_3–MnO_2 displays strong lines due to cryptomelane-like KMn_8O_{16}, as well as weak lines due to α-Mn_2O_3. It is worth noting that this XRD-observed major change in the crystalline bulk structure of calcined KNO_3–MnO_2 is not obviously manifested in the IR spectrum obtained for the material [Fig. 1(*b*)], which does not demonstrate a corresponding switch to the diagnostic absorptions of cryptomelane at 710–700 w, 605–560 m, sh, 530–510 s and 470–450 m, sh cm^{-1}.[14,23] This might be related to the overall weak crystallinity of the material bulk structure (≈40%, see Table 1 below), which

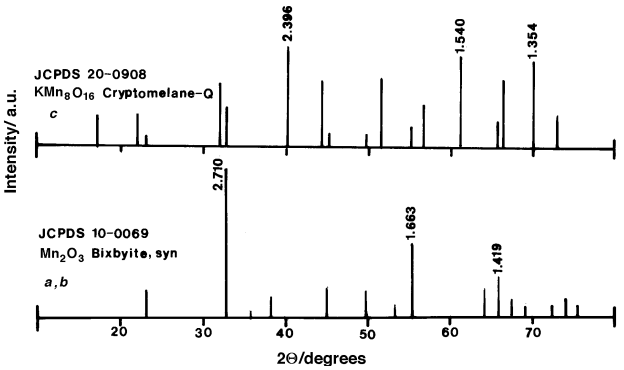

Fig. 2 XRD patterns (CuKα radiation) of the 700 °C calcination products of (*a*) MnO_2 (*b*) $Ba(NO_3)_2$–MnO_2 and (*c*) KNO_3–MnO_2. The *d* spacing (in Å) is given for the strongest three lines in each pattern, as well as the card number of the matching JCPDS standard data

may accordingly mean that initial Mn^{IV}–O species are still in control but in the non-crystalline domain of the bulk. Consistently, the IR spectrum of calcined KNO_3–MnO_2 [Fig. 1(*b*)] is apparently closer in band shape to that of calcined pure MnO_2 [Fig. 1(*a*)], which still includes IR-detectable amounts of non-crystalline Mn_5O_8, than to the standard spectrum of α-Mn_2O_3 [Fig. 1(*d*)].

The above IR and XRD results are further summarized in Table 1, and help to conclude the following: (*i*) the calcination of pure MnO_2 at 700 °C for 2 h decomposes completely the parent oxide, leading to a material bulk consisting of a major proportion of crystalline α-Mn_2O_3 and a minor proportion of the manganoxide-like composition Mn_5O_8 ($Mn^{II}_2Mn^{IV}_3O_8$);[24] (*ii*) the presence of KNO_3 (at 5 wt% K) causes a radical change in the decomposition course of MnO_2, resulting in a material bulk consisting of a major proportion of crystalline cryptomelane-like KMn_8O_{16} $[(V_{2-x}K_x^+)(Mn^{IV}_{8-x}\ Mn^{II}_xO_{16})$ where V is a singly charged cationic vacancy],[25] as well as a minor proportion of crystalline bixbyite-like α-Mn_2O_3 and a trace amount of the manganoxide-like composition Mn_5O_8; and (*iii*) the presence of $Ba(NO_3)_2$ (at 5 wt% Ba) enhances the decomposition of the parent MnO_2 into a material containing α-Mn_2O_3 as the sole detectable crystalline component. Table 1 stresses the fact that the bulk crystallinity for the calcination products is overall modest (40–60%). For simplicity, the calcination products of the pure and impregnated MnO_2 will be referred to below as Mn_2O_3, K-Mn_2O_3 and Ba-Mn_2O_3.

Reactivity of lattice oxygen

Non-cyclic TG curves obtained for Mn_2O_3, K-Mn_2O_3 and Ba-Mn_2O_3 in the gas atmospheres of O_2, CO and CO + O_2 are displayed in Fig. 3. Mn_2O_3 is shown [Fig. 3(A)] to be largely weight-invariant to heating in O_2 up to 950 °C where it decomposes [conceding a *ca.* 3.5% weight loss (WL)] into Mn_3O_4 (WL_{calcd} = 3.4%).[14] This considerable thermal stability of the lattice oxygen in Mn_2O_3 is largely lost on heating in a CO atmosphere at a much lower temperature (≤400 °C). Fig. 3 (A) indicates consistently a *ca.* 10% WL for Mn_2O_3 in CO *via* two fast, strongly overlapping processes: T_{max} = 340 °C (I) and 380 °C (II). The observed WL is very close to

Table 1 Bulk structural characteristics of the calcination products (700 °C, 2 h) of pure and impregnated MnO_2 as obtained from the XRD and IR results

	Calcination product					
					Standard data	
Parent material	Chemical composition	Crystalline structure	Crystallinity[a] /%	Abundance[b]	XRD[c]	IR[d]
MnO_2	Mn_2O_3 +	α-modification; Bixbyite-like	60	j	10–0069	23
	Mn_5O_8	Non-crystalline	—	m	—	14
KNO_3–MnO_2	KMn_8O_{16} +	Double-chain, 2 × 2 channels; Cryptomelane-like	40	j	20–0908	23
	Mn_2O_3 +	α-modification; Bixbyite-like	40	m	10–0069	23
	Mn_5O_8	Non-crystalline	—	t	—	14
$Ba(NO_3)_2$–MnO_2	Mn_2O_3	α-modification; Bixbyite-like	50	s	10–0069	23

[a] Approximated for each crystalline phase by relating the intensity of the strongest observed line to that of a typical crystalline reference.[14] [b] s = sole, d = dominant, j = major, m = minor and t = trace. [c] Card number of corresponding JCPDS standard pattern. [d] Source reference for corresponding standard IR spectrum.

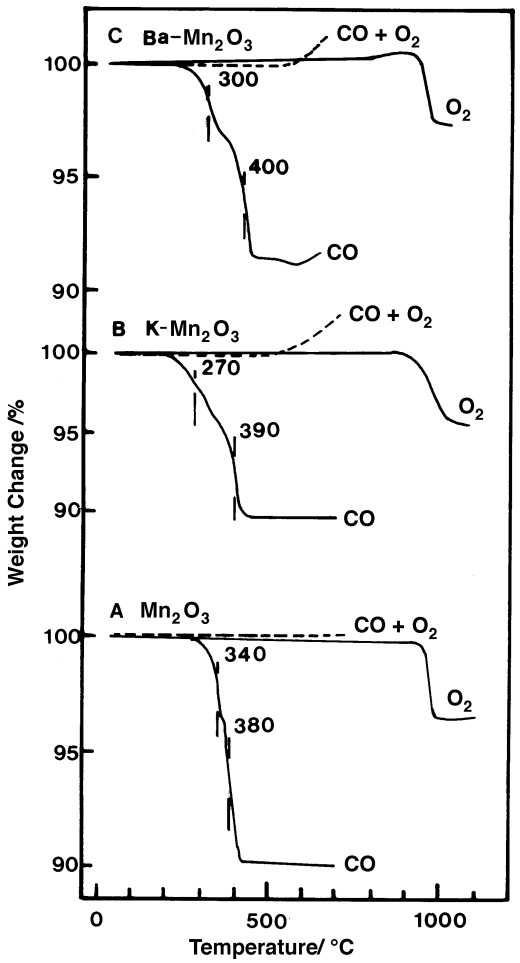

Fig. 3 Non-cyclic TG curves obtained on heating (at 10 °C min^{-1}) the indicated materials (20 ± 1 mg) in a dynamic (50 cm^3 min^{-1}) atmosphere of the individual or mixed gases indicated

that expected (10.2%) for the reductive decomposition of Mn_2O_3 into MnO. The stepwise nature of the reduction course may be related to the composite bulk structure of Mn_2O_3 [α-Mn_2O_3(j) + Mn_5O_8(m), Table 1]. In the mixed gas atmosphere of CO + O_2, where heating was terminated near 700 °C to avoid excessive release of heat, the TG curve [Fig. 3(A)] shows the presence of O_2 to suppress completely the CO reduction of Mn_2O_3. The O_2 atmosphere seems to compensate for the lattice oxygen used up by CO molecules in a catalytic process such as: $2CO(g) + 2O^{2-}(surf) \rightarrow 2CO_2(g) + 4e^-(surf)$ and $O_2(g) + 4e^-(surf) \rightarrow 2O^{2-}(surf)$. The release of CO_2 into the gas phase was chromatographically evidenced in the present investigation. The catalytic conduct of Mn_2O_3 must have commenced at ⩽340 °C to have the reductive decomposition of the bulk suppressed. Indeed, El-Shobaky *et al.*[26] have found Mn_2O_3 species to catalyze CO oxidation in an O_2-rich atmosphere at 100–300 °C.

Fig. 3(B) shows the K alkalization to cause no detectable change in the thermal behaviour of Mn_2O_3 in O_2, except for an earlier enhancement of its decomposition (into Mn_3O_4) near 880 °C, instead of 950 °C for the unmodified oxide [Fig. 3(A)]. The same applies to its reductive decomposition into MnO in a CO atmosphere, which is shown to commence near 180 °C for K-Mn_2O_3, *vs.* 250 °C for Mn_2O_3. Two reductive steps, having different rates, are resolved for K-Mn_2O_3: T_{max} = 270 °C (slow) and T_{max} = 390 °C (fast). This behaviour may also be related to the composite bulk structure assumed by the material [KMn_8O_{16}(j) + α-Mn_2O_3(m) + Mn_5O_8(t), Table 1]. The thermal behaviour of K-Mn_2O_3 in the mixed atmosphere of CO + O_2 is similar to that of the unmodified oxide in assuming a weight-invariant behaviour over the operational temperature range of the reductive decomposition step (*i.e.*, up to 400 °C), but it is different in exhibiting a detectable weight increase at ⩾550 °C. Hence, the K modification does not alter the suppressive influence practised by O_2 molecules on the CO reduction of the material bulk, but it develops a notable capacity towards the uptake of gas molecules from the surrounding atmosphere (most likely CO_2 molecules) at 550–700 °C.

Similar effects are noticed for the Ba alkalization in the TG curves given in Fig. 3(C). The CO reductive decomposition of Mn_2O_3 into MnO is slightly enhanced, and two WL steps of comparable rates are therein resolved: T_{max} = 300 °C and T_{max} = 400 °C. The O_2 suppressive effect on the CO reduction of the material bulk in the CO + O_2 atmosphere remained unchanged, and at ⩾600 °C a slight weight increase is observed. However, two unique effects are also observed for the Ba modification: (*i*) a slight weight gain is effected on heating the oxide at 800–950 °C in an O_2 atmosphere [Fig. 3(C)] and (*ii*) a weight gain commenced to show up on further heating of the oxide reduction product in the CO atmosphere at ⩾600 °C. These two effects appear to be due to a direct involvement of barium sites, rather than to the alkalization of the host manganese oxide. It is obvious from the TG results that the lattice oxygen of Mn_2O_3 constituents [α-Mn_2O_3(j) + Mn_5O_8(m)] enjoys high thermal stability to heating in an O_2 atmosphere up to 950 °C. Thereafter, it is released, leading the solid residue to assume the composition Mn_3O_4 ($Mn^{II}Mn^{III}_2O_4$) at >950 °C. The reversibility of the process involved was evidenced in an earlier investigation.[18] Hence the thermodynamic equilibrium $3\ Mn_2O_3 \rightarrow 2\ Mn_3O_4 + \frac{1}{2}O_2$ is maintained in the presence of an oxygen atmosphere. One may envisage, accordingly, Mn_2O_3 constituents to actively exchange lattice oxygen with the oxygen gas molecules on heating up to 950 °C. When O_2 is replaced by a CO atmosphere, CO molecules pick up lattice oxygen on heating at 350–420 °C, converting Mn_2O_3 into MnO. Thus, it is a reductive process conveying the chemical instability of the lattice oxygen to the reactive CO molecules. The stepwise nature of the reduction course [Fig. 3(A)] may resolve two different types of reducible oxygen in the material: oxygen associated with crystalline (α-Mn_2O_3) and non-crystalline (Mn_5O_8) domains of the bulk. The latter type seems to be the more easily reducible species. The reduction product, MnO, displays no detectable tendency towards further interaction with the gas phase atmosphere (CO or CO_2). The behaviour of Mn_2O_3 constituents in the separate atmospheres of O_2 and CO seems to be maintained in the mixed gas atmosphere of CO + O_2. The active exchangeability of the lattice oxygen with the oxygen gas molecules seems to compensate almost completely for their thermochemical instability in the CO atmosphere, resulting in a weight-invariant behaviour up to 700 °C. These results indicate, moreover, that Mn_2O_3 constituents have no tendency towards high temperature interactions with the gas phase constituents (CO or CO_2).

The alkalization with potassium appears to weaken the lattice oxygen thermal stability to heating in an O_2 atmosphere, probably owing to the formation of KMn_8O_{16} at the expense of the initial constituents of pure Mn_2O_3. A consequent enhancement in the lattice oxygen mobility may be implied from previous reports.[4] The K alkalization also enhances the lattice oxygen reactivity (instability) towards CO molecules, thus invoking a better thermal resolution between the different types of lattice oxygen involved. Lattice oxygen of K-Mn_2O_3 behaves similarly to Mn_2O_3 in the mixed CO + O_2 atmosphere, but develops, unlike Mn_2O_3, a strong tendency towards uptaking of, most likely, CO_2 molecules at ⩾600 °C. So the alkalization with potassium seems to improve the basicity of the lattice oxygen. Apart from the two unique effects described above, which might be attributed to a

direct involvement of Ba sites, the Ba alkalization causes similar changes in the mobility and reactivity of the lattice oxygen of Mn_2O_3.

Fig. 4 compares IR spectra taken from unmodified Mn_2O_3 samples, following heating to 700 °C in O_2, CO or CO + O_2 atmosphere. The figure reveals, in line with the TG results [Fig. 3(A)], no significant differences between the spectra obtained following heating in O_2 and CO + O_2. Both spectra display characteristic bands (at <800 cm^{-1}) of α-Mn_2O_3(j) + Mn_5O_8(m).[14,23] The spectrum obtained following heating in a CO atmosphere shows the reduction of the initial material into MnO, by monitoring the replacement of the initial band structure by a strong blackout absorption below 500 cm^{-1}.[27] These results confirm the suppressive role played by coexisting O_2 molecules on the CO reduction of Mn_2O_3 [Fig. 3(A)]. The weak absorptions at 1401, 1017 and 864 cm^{-1} can help to account for the presence of minute proportions of surface CO_3^{2-} species,[28] thus confirming the inability of MnO to establish bulk carbonate compositions at high temperatures (≥500 °C). Compatibly, $MnCO_3$ is unstable[17] to heating in air at ≥350 °C.

IR spectra taken from K-Mn_2O_3 and Ba-Mn_2O_3 following similar heating in O_2 and CO + O_2 to 700 °C (not shown) were similar to those described above for the unmodified oxide, in maintaining the initial band structure (at <800 cm^{-1}) of each material. In addition, they displayed weak bands (at >800 cm^{-1}) similar to those shown in the spectra exhibited in Fig. 5. These spectra were obtained following the heating of the alkalized Mn_2O_3 materials in CO atmosphere and include (Fig. 5), as a common feature, the blackout absorption characteristic of its reduction into MnO (at <500 cm^{-1}). The spectrum taken from the CO reduced K-Mn_2O_3 displays a number of strong and weak absorptions at 3140, 1633, 1454, 1382, 1131, 857 and 674 cm^{-1}, assignable to $KHCO_3$ and K_2CO_3 species.[28] Analogously, the spectrum taken from the reduction product of Ba-Mn_2O_3 displays bands (at 1755, 1649, 1434, 1116, 850, 691, 565 and 477 cm^{-1}) due to $BaCO_3$ species.[28,29] Thus, the TG-monitored weight

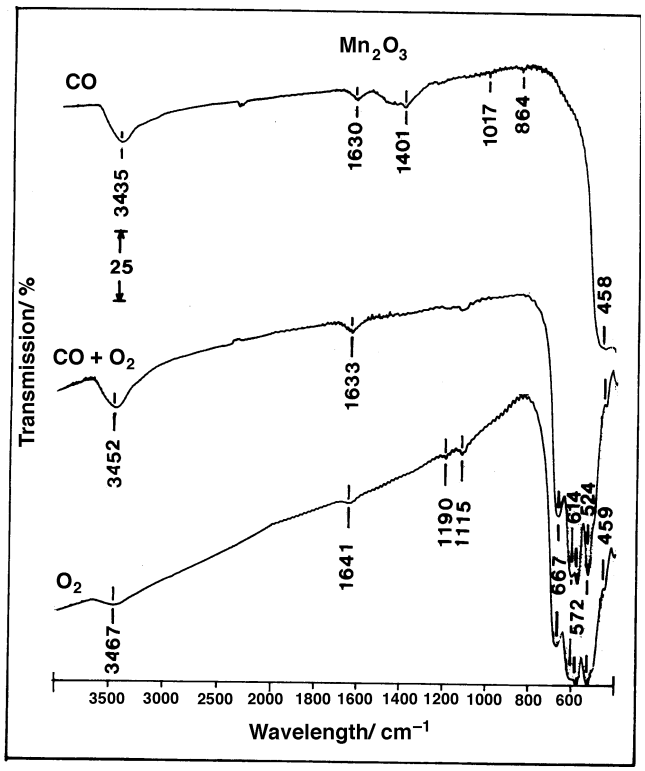

Fig. 4 FT-IR spectra taken from Mn_2O_3 following heating up to 700 °C (at 10 °C min^{-1}) in a dynamic (50 cm^3 min^{-1}) atmosphere of the individual or mixed gases indicated

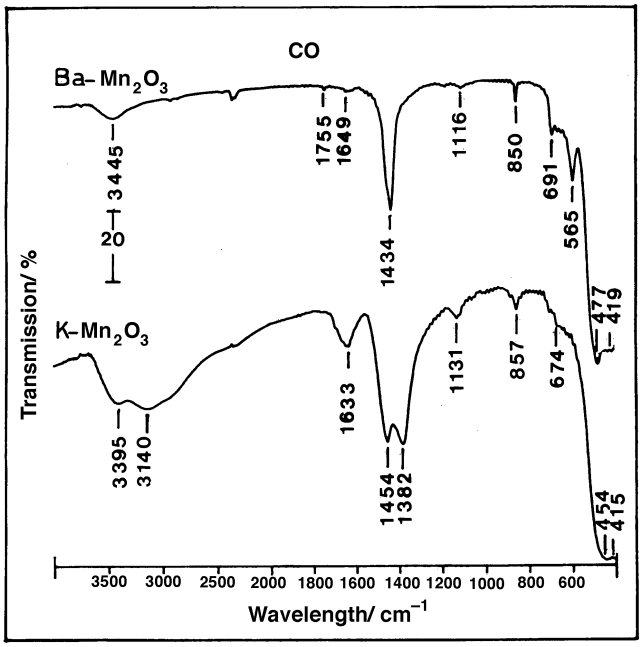

Fig. 5 FT-IR spectra taken from K and Ba alkalized Mn_2O_3 following heating up to 700 °C (at 10 °C min^{-1}) in a dynamic atmosphere (50 cm^3 min^{-1}) of pure CO gas

gain for the modified materials of Mn_2O_3 while heating in CO (or CO + O_2) at >500 °C is due essentially to the uptake by the modifier of the CO oxidation product (*i.e.*, CO_2).

Surface chemical composition

XPS analysis of the surfaces of pure and alkalized Mn_2O_3 monitored C atoms in addition to the expected Mn and O atoms. The binding energy (284.6 eV) of the C(1s) electron emission and the atomic percentage (2.5 ± 0.1%) of the carbon detected attributed its origin to adventitious CH_x contaminant species.[30] Moreover, K atoms were probed on K-Mn_2O_3 and Ba atoms on Ba-Mn_2O_3. Results obtained for all the elements detected, except carbon, are summarized in Table 2. These results indicate a much higher O : Mn atomic ratio (≥3) than expected (≤2) for the bulk composition of the test materials. Thus, the test materials expose oxygen-rich surfaces. The extra-lattice oxygen is due most likely to chemisorbed oxygen and water molecules. The O(1s) electron emission is bi-dispersed. The low-energy electrons (529.8 eV) originate from O^{2-} species,[15,30] whereas the high-energy ones (531.5 eV) arise from OH^- species.[15,30] The broadness of the O^{2-} peak (Table 2) may conceal contributions from other charged oxygen species, whether mono- or binuclear.[15]

On K-Mn_2O_3, an appreciable amount of K atoms has been determined (8.7%). It is probably the large size of the K^+ ions (1.51 Å)[31] that hampers its incursion into the bulk. The presence of K^+ ions seems to enrich the electron density around the surface oxygen species, since the binding energies determined for both O^{2-} (529.5 eV) and hydroxyl oxygen (531.2 eV) are slightly lower than the corresponding energies determined for Mn_2O_3 (Table 2). Meanwhile, the Mn sites are rendered electron-poor as compared to similar sites on the K-free material (Table 2). A similar effect can be seen on Ba-Mn_2O_3, as regards the Mn sites. However, considering the surface oxygen species, the Ba^{2+} additives seem to decrease the electron density about these sites (Table 2), in contrast to the K^+ additives. Also unlike K^+, the surface concentration of Ba^{2+} ions is minute (1.2%). Thus, most of the barium additives seem to reside in the bulk, though the ionic radius of Ba^{2+} (1.49 Å)[31] is not much less than that of K^+. It is worth mentioning that when values of the surface atom% of K (8.7%) and Ba

Table 2 Surface chemical composition of pure and alkalized Mn_2O_3 as probed by XPS

	BE/eV									
	Ba(3d)			Mn(2p)				K(2p)		
Test material	3/2	5/2	%[a]	1/2	3/2	%[a]	O(1s) FWHM[b]	1/2	3/2	%[a]
Mn_2O_3	—	—	—	653.2	641.6	24.1	531.5(2.2) 529.8(2.0)	—	—	—
K-Mn_2O_3	—	—	—	653.6	642.0	20.3	531.2(1.8) 529.5(2.0)	295.0	292.2	8.7
Ba-Mn_2O_3	795.4	780.0	1.2	653.6	642.0	21.2	531.8(2.2) 530.0(1.8)	—	—	—

[a] Atomic percent. [b] Full width at half maximum in eV.

(1.2%) are compared to the respective bulk values (4% for K and 1% for Ba), as derived from the chemical composition of the materials, one may conclude that the partition of K and Ba in the solids is similarly rather homogeneous.

Surface oxygen species

The XPS analysis results (Table 2) account for the presence on the pure and alkalized Mn_2O_3 of charged oxygen atoms and hydroxyl oxygen (OH^-). This can be further revealed from the deconvoluted peaks of O(1s) electron emissions, as shown in Fig. 6. The relative peak area attributes *ca.* 80% of the total amount of surface oxygen to charged oxygen atoms. Table 2 results indicate that the modification with potassium improves the nucleophilicity of surface oxygen, whereas the modification with barium improves its electrophilicity.

Table 3 compares the oxygen (V_m^O) and CO (V_m^{CO}) chemisorption capacities of pure and alkalized Mn_2O_3. The table also presents the nitrogen physisorption capacity (V_m^N) of the materials, whereby they are shown to exhibit surfaces having a low BET area ($\approx$7–10 $m^2\ g^{-1}$) and a low heat of adsorption ($C_{BET} \leqslant 500$).[32] It is obvious that the CO chemisorption capacity of the test materials are generally less than that of nitrogen adsorption. This emphasizes the specific nature of the CO adsorption. It has been established that CO chemisorption on metal oxide surfaces is feasible only at low temperatures[33] and occurs *via* bonds dominated by donation of CO 5σ electrons to surface Lewis acid sites (coordinatively unsaturated metal sites).[33] The results (Table 3) show that the alkalization of Mn_2O_3, particularly with potassium, reduces the CO chemisorption capacity. This can be effected by lowering the surface Lewis acidity and/or concentration of adsorbing sites (coordinatively unsaturated Mn ions). The XPS results showing higher Mn(2p) binding energies and lower Mn atomic percentage for the alkalized than for the pure Mn_2O_3 (Table 2) may support the latter attribution.

The oxygen chemisorption capacity of pure Mn_2O_3 is much less even than its CO chemisorption capacity ($V_m^O/V_m^{CO} = 0.19$). The alkalization, particularly with potassium, improves markedly the oxygen chemisorption capacity ($V_m^O/V_m^{CO} = 3.82$ for K-Mn_2O_3). In contrast to CO chemisorption, oxygen chemisorption on metal oxide surfaces is enhanced at high temperatures[1,2,6] and occurs *via* bonds dominated by donation of electrons of surface sites (oxide sites) to anti-bonding orbitals of O_2. The XPS observation of the K influenced decrease of the binding energy of O(1s) electrons (Table 2) may attribute the K improved chemisorption of oxygen to the improved electron density of the adsorbing sites.

Cyclic TG curves obtained in an oxygen atmosphere demonstrated that following an initial heating of the test materials between 500 and 900 °C, a cooling within the same temperature range causes a *ca.* 1% weight gain, and a sub-

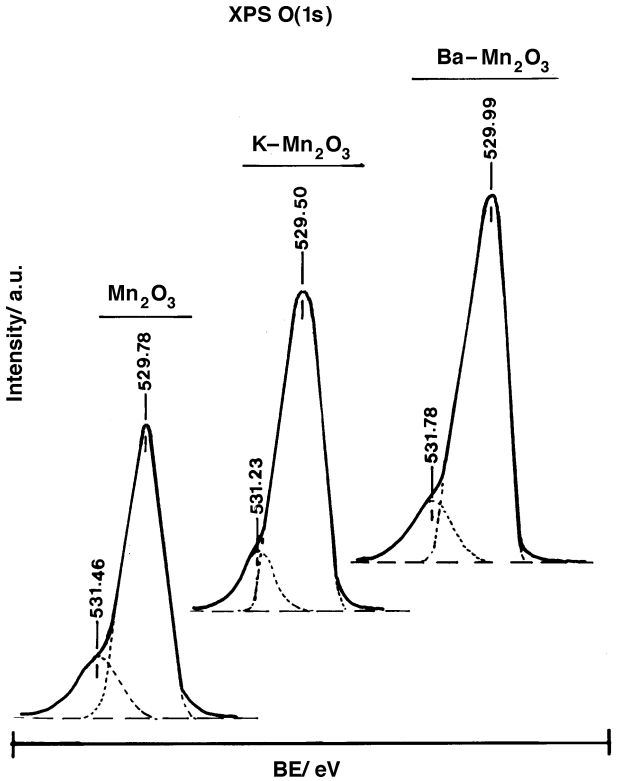

Fig. 6 X-ray O(1s) photoelectron emission spectra exhibited by the indicated materials

Table 3 N_2 determined surface area ($S_{BET}/m^2\ g^{-1}$), the monolayer capacity [V_m/cm^3 (NTP) g^{-1}] and the concentration (σ/molecule per 100 Å^2) of irreversibly adsorbed CO (at −196 °C) and O_2 (at 200 °C) on pure and alkalized Mn_2O_3

	N_2			CO			O_2			
Test material	V_m^N	S_{BET}	C_{BET}	V_m^{CO}	σ	V_m^{CO}/V_m^N	V_m^O	σ	V_m^O/V_m^N	V_m^O/V_m^{CO}
Mn_2O_3	1.55	6.7	420	0.71	2.8	0.46	0.13	0.5	0.009	0.19
K-Mn_2O_3	2.35	10.2	51	0.10	0.3	0.04	0.39	1.0	0.17	3.82
Ba-Mn_2O_3	2.18	9.5	119	0.38	1.1	0.17	0.30	0.9	0.14	0.79

Table 4 Kinetic parameters for the catalytic decomposition of an H_2O_2 solution at different temperatures (20–35 °C) on pure and alkalized Mn_2O_3

Test material	Specific rate constant k_s /s^{-1} (g catalyst)$^{-1}$		Activation energy E_a /kJ mol^{-1}	Intrinsic rate constant k_i /10^3 s^{-1} (m^2 catalyst)$^{-1}$ g^{-1}	
	25 °C	30 °C		25 °C	30 °C
Mn_2O_3	0.352	0.499	77.1	52.3	74.1
K-Mn_2O_3	0.380	0.390	23.2	37.0	38.0
Ba-Mn_2O_3	0.660	0.778	19.5	69.5	81.9

sequent heating—still within the same temperature range—results in a *ca.* 1% weight loss. A further heating–cooling cycle gave the same weight changes, thus confirming the reversibility of the process(es) involved. The set of cyclic TG curves obtained for pure Mn_2O_3 is shown in Fig. 7; it shows a weight loss amounting to *ca.* 3.7% in the initial heating up to 900 °C. It is worth noting that this initial weight loss, which was not observed for the doped samples, was monitored by the non-cyclic TG of the pure oxide [Fig. 3(A)] but at a lesser magnitude (≈1%). Although the weight loss process(es) involved must relate to the same origin (most likely the non-crystalline component of the material, Table 1, the disagreement between the weight loss values determined might be due to the diverse heat supply dissipation rates imposed on the test material by the different modes (cyclic and non-cyclic) of the measurements applied. The minute weight changes determined following the initial heating up to 900 °C confine the occurrence of the process(es) involved to the gas/solid interface, and, consequently, attribute the weight gain to oxygen adsorption and the weight loss to oxygen desorption. The fact that the weight gain is observed on cooling at 900–500 °C means that the oxygen adsorption in this temperature range is not an activated process, and that the test materials themselves assume already oxygen-rich surfaces (*vide supra*). This may justify the modesty of oxygen chemisorption on the test samples (Table 3). Carrott and Sheppard[34] have found, by IR spectroscopy, that oxygen adsorbed on oxygen-rich surfaces is comprised essentially of charged molecular species (O_2^{x-}), which are described[1,2,6] as being electrophilic in comparison to the dissociatively adsorbed O^- and O^{2-} species. It is these electrophilic oxygen species that are considered to be the active surface intermediates in deep oxidation processes,[6] whereas the nucleophilic oxygen is thought to catalyze oxidation reactions selectively.[6]

H_2O_2 decomposition activity

Table 4 summarizes the Arrhenius kinetic parameters for the catalytic decomposition of H_2O_2 solutions on the test materials. The results show consistent trends of variation in both the specific (per g catalyst) and intrinsic (per m^2 catalyst) rate constants at a given reaction temperature. The activation energies determined help rank the test materials in the following ascending order of catalytic activity: Mn_2O_3 < K-Mn_2O_3 < Ba-Mn_2O_3. Thus, the alkalization of Mn_2O_3 develops the required surface electron-mobile environment for the H_2O_2 decomposition.[35–37] It has been established[35,36] that a proportionate electron acceptor–donor behaviour of a catalytic surface optimizes the decomposition kinetics of H_2O_2. This seems to be the case for Ba-Mn_2O_3, which facilitates the lowest activation energy reaction pathway (Table 4). The increase of the V_m^O/V_m^{CO} ratio from 0.19 (Mn_2O_3) to 0.79 (Ba-Mn_2O_3) is accompanied by a considerable decrease in the activation energy of the reaction from 77.1 to 19.5 kJ mol^{-1}. A further, but considerable, increase in the V_m^O/V_m^{CO} ratio to 3.82 (K-Mn_2O_3) is conversely accompanied by an increase of the activation energy from 19.5 to 23.2 kJ mol^{-1}. Assuming that the ratio V_m^O/V_m^{CO} mirrors the proportion of electron donor/electron acceptor properties of the surface, Ba-Mn_2O_3 seems to generate the optimal electron-mobile environment for the catalytic decomposition of H_2O_2.[35–37]

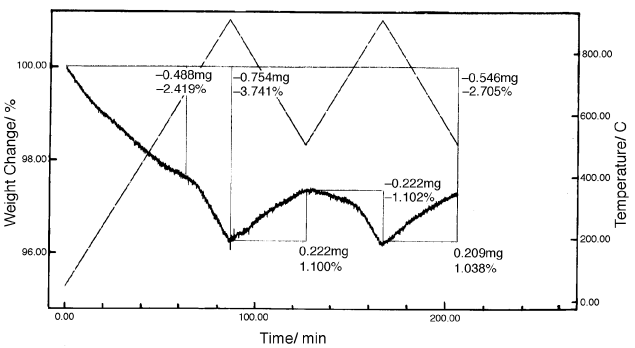

Fig. 7 Cyclic TG curves obtained for pure Mn_2O_3 following two heating-cooling cycles performed at 500–900 °C in 50 cm^3 O_2 min^{-1}

Conclusions

The above presented and discussed results indicate that alkalization of a material bulk consisting of α-Mn_2O_3(j) + Mn_5O_8(m) with 5 wt% potassium or barium ion additives converts the bulk composition into KMn_8O_{16}(j) + α-Mn_2O_3(m) or α-Mn_2O_3, respectively. Consequently, the electron density and the mobility of lattice and surface oxygen species are improved. Moreover, the bulk thermochemical instability to heating in a CO atmosphere is increased and a capacity towards CO_2 uptake is developed. Furthermore, the surface catalytic behaviour towards CO oxidation in the gas phase is maintained, whereas the behaviour towards H_2O_2 decomposition in the liquid phase is considerably promoted.

Acknowledgements

The authors acknowledge with appreciation the financial support of Kuwait University under research project SC 076 and general facility projects SLC 056, SLC 063 and SLD 002, as well as the excellent technical assistance at Analab of the Chemistry Department.

References

1 M. Che and A. J. Tench, *Adv. Catal.*, 1982, **31**, 77.
2 M. Che and A. J. Tench, *Adv. Catal.*, 1983, **32**, 1.
3 H. Kung and M. Kung, *Adv. Catal.*, 1984, **33**, 159.
4 P. J. Gellings and H. J. M. Bouwmeester, *Catal. Today*, 1992, **12**, 1.
5 A. Bielanski and J. Haber, *Catal. Rev.-Sci. Eng.*, 1979, **19**, 1.
6 A. Bielanski and J. Haber, *Oxygen in Catalysis*, Marcel Dekker Inc., New York, 1991.
7 R. Prasad, L. A. Kennedy and E. Ruckenstein, *Catal. Rev.-Sci. Eng.*, 1984, **26**, 1.
8 F. Nakajima, *Catal. Today*, 1991, **10**, 1.
9 G. Mul, J. P. A. Neeft, F. Kapteijn, M. Makkee and J. A. Moulijn, *Appl. Catal. B: Environ.*, 1995, **6**, 339.

10 T. Yamashita and A. Vannice, *J. Catal.*, 1996, **163**, 158.
11 Y. Hirao, C. Yokoyama and M. Misono, *Chem. Commun.*, 1996, **5**, 597.
12 J. G. Wu, S. B. Li, J. Z. Niu and X. P. Fang, *Appl. Catal. A: Gen.*, 1995, **124**, 9.
13 F. Kapteijn, L. Singoredjo, N. J. J. Dekker and J. A. Moulijn, *Ind. Eng. Chem. Res.*, 1993, **32**, 445.
14 A. K. H. Nohman, M. I. Zaki, S. A. A. Mansour, R. B. Fahim and C. Kappenstein, *Thermochim. Acta*, 1992, **210**, 103.
15 M. I. Zaki and C. Kappenstein, *Z. Phys. Chem.*, 1992, **176**, 97.
16 R. L. Segall, R. S. C. Smart and P. S. Turner, in *Surface and Near Surface Chemistry of Oxide Materials*, ed J. Nowotny and L-C. Dufour, Elsevier, Amsterdam, 1988, pp. 527–576.
17 M. I. Zaki, A. K. H. Nohman, C. Kappenstein and T. M. Wahdan, *J. Mater. Chem.*, 1995, **5**, 1081.
18 M. I. Zaki, M. A. Hasan, L. Pasupulety and K. Kumari, *Thermochim. Acta*, 1997, **311**, 97.
19 K. Taylor, in *Catalysis Science and Technology*, ed. J. R. Anderson and M. Boudart, Springer-Verlag, Berlin, 1984, vol. 5, pp. 119–170.
20 J. Deren, J. Haber, A. Podgorecka and J. Burzyk, *J. Catal.*, 1963, **2**, 161.
21 I. M. Campbell, *Reaction Kinetics*, Blackie, Glasgow, 1980, pp. 1–12.
22 N. T. McDevitt and W. L. Baun, *Spectrochim. Acta*, 1964, **20**, 799.
23 R. M. Potter and G. R. Rossman, *Am. Mineral.*, 1979, **64**, 1199.
24 W. Feitknecht, *Pure Appl. Chem.*, 1964, **9**, 423.
25 C. Frondel, U. B. Marvin and J. Ito, *Am. Mineral.*, 1960, **45**, 871.
26 G. A. El-Shobaky, G. A. Fagal, A. M. Ghozza and M. A. Shouman, *Mater. Lett.*, 1994, **19**, 225.
27 F. Vratny, M. Dilling, F. Gugliotta and C. N. R. Rao, *J. Sci. Ind. Res., Sect. B*, 1961, **20**, 590.
28 F. A. Miller and C. H. Wilkins, *Anal. Chem.*, 1952, **24**, 1253.
29 F. A. Miller, G. L. Carlson, F. F. Bentley and W. H. Jones, *Spectrochim. Acta*, 1960, **16**, 135.
30 C. D. Wagner, N. M. Riggs, L. E. Davis and J. J. Moulder, in *Handbook of X-ray Photoelectron Spectroscopy*, ed. G. E. Mullenberg, Perkin-Elmer, Minnesota, 1979.
31 R. D. Shannon, *Acta Crystallogr., Sect. A*, 1976, **32**, 751.
32 S. J. Gregg and K. S. W. Sing, *Adsorption, Surface Area and Porosity*, Academic Press, London, 1967, pp. 35–114.
33 M. I. Zaki and H. Knözinger, in *Proceedings of the 2nd International Conference on Chemical Reaction Engineering*, Wiley-Eastern, New Delhi, 1987, pp. 19–30.
34 P. J. M. Carrott and N. Sheppard, *J. Chem. Soc., Faraday Trans. 1*, 1983, **79**, 2425.
35 G-M. Schwab and S. B. Kanungo, *Z. Phys. Chem.* (*Munich*), 1977, **107**, 109.
36 P. Lahiri and S. K. Sengupta, *Can. J. Chem.*, 1991, **69**, 33.
37 J. R. Goldstein and A. C. C. Tseung, *J. Catal.*, 1974, **32**, 452.

Received in Montpellier, France, 12th January 1998;
Paper 8/00796I